

Supplementary wavelength calibration methods for SALT/RSS spectropolarimetric observations

Justin Cooper
B.Sc. (Hons)

Submitted in fulfillment of the requirements for the degree
Magister Scientiæ
in the Faculty of Natural and Agricultural Sciences
Department of Physics
University of the Free State
South Africa

Date of submission: January 8, 2024

Supervised by: Prof. B. van Soelen, Department of Physics

Abstract

TODO:

- Done last
- Flow from use of SALT and pipeline and basics of its science implementations into why a more streamlined wavelength calibration is an improvement.
- Give summary of results.
- Aim for a paragraph (~ 600) without going too in-depth into anything specific.
- Brian's comment: Abstract should summarize paper. Include results, conclusions, etc.

Keywords:

TODO:

- Add Keywords \rightarrow look up the astronomy journal keywords
- Look up keywords for pipeline development and data reduction.
- I.E. Polarization: optical, Calibration: wavelength, galaxies: AGN, Blazars, Pipeline, SALT, etc.

Contents

1	Introduction	5
2	Spectropolarimetry and the SALT RSS	7
2.1	Spectroscopy	7
2.1.1	Telescope optics	7
2.1.2	Slit	8
2.1.3	Collimator	8
2.1.4	Dispersion Element	8
2.1.5	Lens	9
2.1.6	Detector	9
2.1.7	Dispersion of Light	9
2.1.8	Detector and Spectroscopic Calibrations	13
2.2	Polarimetry	19
2.2.1	Polarization	20
2.2.2	Polarization Measurement	22
2.2.3	Polarimetric calibrations	26
2.3	Spectropolarimetry	27
2.3.1	Spectropolarimetric measurement	28
2.3.2	Spectropolarimetric calibrations	29
2.4	The Southern African Large Telescope	30
2.4.1	The primary mirror	30
2.4.2	Tracker and tracking	31
2.4.3	SALT Instrumentation	32
2.5	RSS Spectropolarimetry	33
2.5.1	POLSALT	34
3	Developed Tools	37
3.1	Limitations of POLSALT and the Need for a Supplementary Tool	37
3.2	Wavelength calibrations using the Supplementary Pipeline and IRAF	38
3.2.1	Splitting the uncalibrated wavelength files	38
3.2.2	IRAF wavelength calibration	38
3.2.3	Joining the wavelength calibrated files	38
3.3	Additional Tools	38
3.3.1	Cross correlation	38
3.3.2	Skyline comparisons	38
3.4	General Reduction Procedure	38
4	Testing	39

5	Science Applications	41
5.1	Application to Spectropolarimetric Standards	41
5.2	Application in publications	41
6	Conclusions	43
	List of Acronyms	45
	Bibliography	47

Chapter 1

Introduction

TODO: Very short intro to Spectroscopy, Polarisation, and Spectropolarisation and their Importance in astronomy

TODO: Problem Statement, VERY IMPORTANT, roughly a sentence but problem thoroughly fleshed out.

TODO: Focus on AGN implications and implementations such as the types of objects and a short history for each type of object, Blazar focus with specification on BL Lacs and FSRQs, the Unified Model, ~~The Blazar sequence~~

TODO: Brian's comment: Highlight importance of polarimetry for understanding emission and how that plays a role in AGN.

TODO: Basics of modelling (Different energy/wavelength ranges used and what the models tell us about emission processes/structure) so that Hester's results can be noted for applications of the pipeline.

TODO: General layout of Dissertation

Chapter 2

Spectropolarimetry and the SALT RSS

This chapter gives an overview of the basics of spectropolarimetry (§ 2.3), and how it functions, following from the principles of both spectroscopy (§ 2.1) and polarimetry (§ 2.2). Further, it is discussed how these techniques are practically implemented for Southern African Large Telescope (SALT) (§ 2.4), more specifically the Robert Stobie Spectrograph (RSS) (§ 2.4.3), and how the spectropolarimetric reduction process is completed (§ 2.5).

2.1 Spectroscopy

Spectroscopy originated in its most basic form with Newton’s examinations of sunlight through a prism (Newton and Innys, 1730) but came to prominence as a field of scientific study with Wollaston’s improvements to the optics elements (Wollaston, 1802), Fraunhofer’s use of a diffraction grating instead of a prism (der Wissenschaften, 1824), and Bunsen and Kirchhoff’s classifications of spectral features to their respective chemical elements (Kirchhoff and Bunsen, 1861).

The simplest spectrometer schematic, as shown in Figure 2.1, consists of incident light collected from the telescope’s optics, labelled A, being focused onto a slit, B, and passed through a collimator, C. The collimator collimates the light allowing a dispersion element, D, to disperse the light into its constituent wavelengths. The resultant spectrum is focused by a lens, E, onto a focal plane, F. Viewing optics are situated at the focal plane in the case of a spectroscope and a detector is situated at the focal plane in the case of a spectrograph.

2.1.1 Telescope optics

The telescope optics refers simply to all the components of a telescope necessary to acquire a focal point at the spectrometer entrance, labelled B. The focal point in most traditional telescope designs is fixed relative to the telescope and so the spectrometer may be mounted at that point. In cases where the telescope is designed to have a moving focal point relative to the telescope (see Buckley et al., 2006; Cohen, 2009; Ramsey et al., 1998), the spectrometer must also move along the telescope’s focal path.



Figure 2.1: Layout depicting the light path through a spectrometer.

2.1.2 Slit

The slit's function is to control the amount of incident light entering a spectrometer and, along with the exposure time of the detector, prevents over-exposures of bright sources on highly sensitive detectors (Tonkin, 2013). If a source is spatially resolvable, or larger than the seeing conditions, the slit further acts to spatially limit the source to increase the spectral resolution, resulting in sharper features in the resultant spectrum. Without the slit the spectral resolution would be determined by the projected width of the source on the detector, or the seeing if the source was a star-like point source. Increasing the spectral resolution comes with the trade-off of decreasing the light collected from the source and thus acquiring a less intense resultant spectrum. Multiple spectra may be acquired simultaneously when the slit is positioned such that collinear sources lie along the slit.

2.1.3 Collimator

The collimator's function is to collimate the focused light from the telescope, ensuring that all light rays run parallel before reaching the dispersion element. Since the collimator accounts for the telescope's focus, the focal ratio of the collimator (f_c/D_c , where f refers to the focal length and D refers to the diameter) should thus ideally match the focal ratio of the telescope (f_T/D_T). Another consideration of the collimator is ensuring that the full collecting area is utilized as an oversized collimator may be heavier as well as more expensive than necessary.

2.1.4 Dispersion Element

Including a dispersion element in the optical path is what defines a spectrometer. As the name suggests, a dispersion element disperses the light incident on it into its constituent wavelengths and produces a spectrum. There are two types of dispersion elements, namely the prism and the diffraction grating, which operate on different principles, as discussed in § 2.1.7.

2.1.5 Lens

The lens functions similarly to that of the telescope's optics but in this case focuses the dispersed light onto a receiver situated at the focal plane. As mentioned previously, an eye piece is fixed to the focal point for a spectroscope while a spectrograph employs a detector.

2.1.6 Detector

The two most prevalent detector types in spectroscopy are the Charged-Coupled Device (CCD) and Complementary Metal-Oxide-Semiconductor (CMOS) detectors. In astronomical spectroscopy however, sources are fainter and exposure times are much longer and so the CCD detectors are by far the preferred detector as their output has a higher-quality and lower-noise when compared to CMOS cameras under the same conditions (Janesick et al., 2006).

The CCD is a detector composed of many thousands of pixels which can store a charge so long as a voltage is maintained across the pixels. Each pixel detects incoming photons using photo-sensitive capacitors through the photoelectric effect and converts the photons to a charge (Buil, 1991). There are also thermal agitation effects which introduce noise to the charge accumulated by a pixel, further discussed in § 2.1.8. Once the exposure is finished the accumulated charge is read column by column, row by row, through an Analog-to-Digital Converter (ADC) which produces a two-dimensional array of 'counts' with which information may be extracted from.

2.1.7 Dispersion of Light

Light can be broken up into its constituent wavelengths through two different physical phenomena, namely dispersion and diffraction, which dispersive elements use to create spectra. Dispersive prisms and diffractive gratings each have their strengths and weaknesses and a wide spectrum of instruments exist implementing both, or either, concepts. Regardless of the specific element, dispersive elements all have a resolving power, R , and an angular dispersion. Generally, while the angular dispersion is a more involved process to determine, the resolving power of a spectrograph can be measured as:

$$R = \frac{\lambda}{FWHM} \quad (2.1)$$

where λ is the wavelength of an incident monochromatic beam and $FWHM$ refers to the width of the feature on the detector at half of its maximum intensity.

Prism

The prism operates on the principle that the refractive index of light, n , varies as a function of its wavelength, λ . Prisms were the only dispersive elements available for early spectroscopic studies, but they were not without flaw. The angular dispersion of a prism is given by

$$\frac{\partial \theta}{\partial \lambda} = \frac{B}{a} \frac{dn}{d\lambda} \quad (2.2)$$

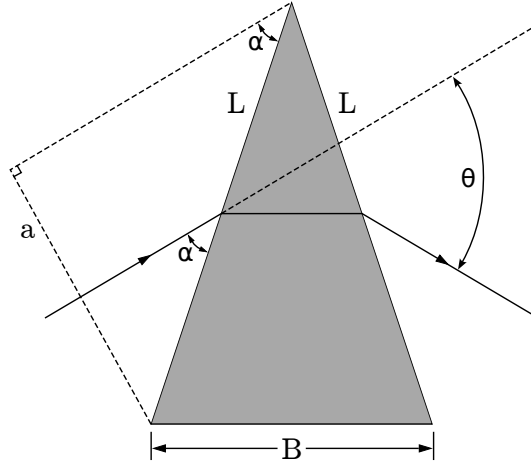


Figure 2.2: Geometry of a prism refracting an incident monochromatic beam at a minimum deviation angle.

where θ is the angle at which the refracted light differs from the incident light, λ is the wavelength of the incident light, B is the longest distance the beam would travel through the prism, and $a = L \sin(\alpha)$ is the cross-section of the incident beam where L is the length of the transmissive surfaces and α is the incident angle of light to the prism surface, as shown in Figure 2.2. The refractive index of a material as a function of its wavelength, $n(\lambda)$, can be approximated by Cauchy's equation

$$n(\lambda) = A_C + \frac{B_C}{\lambda^2} + \frac{C_C}{\lambda^4} + \dots \quad (2.3)$$

where A_C, B_C, C_C are the Cauchy coefficients and have known values dependent on the material. Cauchy's equation is a much simpler approximation of the refractive index that remains very accurate at visible wavelengths. Taking only the first term of the derivative of the Cauchy equation allows us to approximate the angular dispersion of a prism.

$$\frac{\partial \theta}{\partial \lambda} = -\frac{B}{a} \frac{2B_C}{\lambda^3} \propto -\lambda^{-3} \quad (2.4)$$

Equation 2.4 shows that the angular dispersion of a prism is wavelength dependent and furthermore that longer wavelengths are dispersed less than shorter wavelengths (Birney et al., 2006; Hecht, 2017). The dependence of the angular dispersion, $d\theta/d\lambda$, on the wavelength, λ , is crucial for the formation of a spectrum but this cubic, non-linear, relation results in a non-linear spectrum. Since prisms rely on the refractive index of the material they are made of, they have low angular dispersions.

Multiple prisms can be used to increase the angular dispersion but as the dispersion is non-linear it becomes increasingly more difficult to calibrate. The more material and material boundaries the light must pass through, the more its intensity decreases due to attenuation effects and Fresnel losses. Even so, the transmittance of modern prisms for their selected wavelength range is generally very high¹ due to improved manufacturing methods as well as improved transmitting materials.

¹See manufacturers technical specifications, THORLABS, or Edmund Optics for example.



Figure 2.3: Geometry of a reflective blazed grating refracting an incident monochromatic beam.

Diffraction grating

The alternative dispersing element is a diffraction grating, which operates on the principle that as light interacts with a grating where the groove size is comparable to the light's wavelength, the light is dispersed through constructive and destructive interference. This interference results in multiple diffracted beams m , called orders, either side of a central reflected, or transmitted, beam such that $m \in \mathbb{Z}$, where $m = 0$ is the non-dispersed, or reflected, beam.

An example of a reflective blazed grating is illustrated in Figure 2.3. Here a monochromatic beam is incident on the grating at an angle of α from the grating normal. Due to the interference, the beam of wavelength λ is found at an angle of β from the grating normal. The relation between the incident and diffracted beams is given by the grating equation

$$m\lambda = \sigma(\sin(\alpha) \pm \sin(\beta)) \quad (2.5)$$

where σ is the groove spacing of the grating and m is the order of the diffracted beam being considered. The grating equation also applies to transmission gratings, though care should be taken for the signs of α and β .

Equation 2.5 also shows that different wavelengths will have the same angle of dispersion. The regions of an order that do not overlap with another order are called free spectral ranges. To account for the overlaps and increase the free spectral range an order-blocking filter may be used. A diffraction grating may be blazed by an angle, θ , such as in Figure 2.3. Blazing refers to the fact that the grooves on the surface of the grating are not symmetrical. The asymmetry of the grooves diffract the incident beam such that most of the incident beam's intensity is found in a single order. The wavelength at which a blazed spectrograph is most effective is called the blaze wavelength, λ_b , which is determined by

$$m\lambda_b = 2\sigma \sin(\theta) \cos(\alpha - \theta) \quad (2.6)$$

where

$$2\theta = \alpha + \beta. \quad (2.7)$$

Taking the derivative of Equation 2.5 with respect to λ while keeping α constant, allows us to determine the angular dispersion of a diffraction grating, namely

$$\frac{\partial \beta}{\partial \lambda} = \frac{m}{\sigma \cos(\beta)}. \quad (2.8)$$

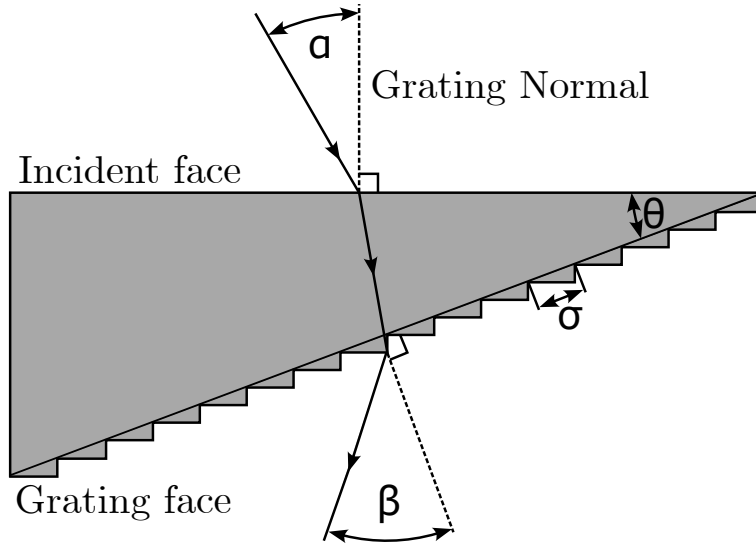


Figure 2.4: Diagram of a grism for an incident monochromatic beam of light and a diffracted beam of order $m = 1$.

Substituting m/σ with the grating equation gives

$$\frac{\partial \beta}{\partial \lambda} = \frac{\sin(\alpha) + \sin(\beta)}{\lambda \cos(\beta)} \propto \lambda^{-1}. \quad (2.9)$$

Similarly to the dispersion of a prism, Equation 2.9 shows that the dispersion of a grating is wavelength dependent, but this dependence is only inversely proportional and thus more uniform across a wavelength range than that of a prism. Furthermore, shorter wavelengths are refracted less than longer wavelengths since there is no negative relation between the angular dispersion and the wavelength (Birney et al., 2006; Hecht, 2017).

As mentioned before, multiple subgroups exist for both dispersive prisms and diffractive gratings. For prisms, along with the single and multiple prism setups mentioned, there also exists grisms and immersed gratings. A grism (Grating Prism), as shown in Figure 2.4, refers to a transmissive grating etched onto one of the transmissive faces of a prism and allows a single camera to capture both spectroscopic and photometric images without needing to be moved, with and without the grism in the path of the beam of light, respectively. An immersed grating refers to a grism modified such that the transmissive grating is coated with reflective material. The primary source of dispersion for both grisms and immersive gratings is the grating and any aberration effects from the prism are negligible in comparison.

Other types of gratings include the Volume Phase Holographic (VPH) grating as well as the echelle grating. The VPH grating consists of a photoresist, which is a light-sensitive material, sandwiched between two glass substrates. Diffraction is possible since the photoresist's refractive index varies near-sinusoidally perpendicularly to the grating lines, as seen in Figure 2.5. This allows for sharper diffraction orders and low stray light scattering as compared to more traditional gratings but since blazing is not possible the efficiency is decreased. An echelle grating refers to a diffraction grating with higher groove spacing which is optimized for use at high orders. The high order of the diffracted beam allows for greater angular dispersion which is most useful when combined with another dispersion element to cross-disperse a spectrum, resulting in a high resolution spectrum.



Figure 2.5: Diagram of a VPH grating for an incident monochromatic beam of light.

2.1.8 Detector and Spectroscopic Calibrations

Acquiring a spectrum from observations is more involved than simply reading out the data recorded on the CCD. A raw science image, which is the raw counts of the observed source read from the CCD with no calibrations applied, has on it a combination of useful science data as well as noise. The noise is a combination of random noise introduced through statistical processes and systematic noise introduced through the instrumentation and the observation conditions the source was observed under. This noise causes an uncertainty in the useful data and can be minimized, predominantly by calibrating for the systematic noise, but never fully removed (Howell, 2006).

The dominant source of noise in a raw image is detector noise. CCDs are manufactured to have a small base charge in each pixel, called the ‘bias’ current which allows the readout noise, a type of random noise, to better be sampled. There is also an unintentional additional charge which is linearly proportional to the exposure time and originates from thermal agitation of the CCD material, called the ‘dark’ current. The dark current can be minimized and possibly ignored if the CCD is adequately cooled. These types of noise add to the charge held by a pixel and are thus considered additive.

The CCD is not a perfect detector and the efficiency of it and the optics of the telescope also contribute noise to the image. The efficiency of a CCD is referred to as the Quantum Efficiency, and it is a measure of what percentage of light striking the detector is actually recorded and converted to a charge. The efficiency of the CCD and telescope optics is also wavelength dependent and so the noise that results from them is more complex than that of additive noise. This type of noise is referred to as multiplicative noise.

Additive noise, such as bias and dark currents, is inherent to CCD images, and as such needs to be subtracted out first when performing calibrations. Bias currents can be found by taking a bias image or by adding an overscan region to each image. A bias image is an image where the charges on the CCD are reset and then immediately read off without exposing anything on the detector, effectively taking an image with zero exposure time. Alternatively, to save time during an observational run, overscan regions may be added to the images. An overscan region refers to adding a few cycles to the readout of each



Figure 2.6: Diagram of a CCD. Figure adapted from (Litwiller, 2001)

column of the CCD such that the base current is read out and appended to each image.

Dark currents can be found by taking an image with nothing exposed onto the detector for a certain exposure time. This resultant dark image can then be scaled to the science images exposure time since the dark current should be linearly proportional to exposure time. When the detector is capable of being held at precise temperatures, dark images may be taken over multiple hours during the day to produce a high quality master dark image that may then be scaled and subtracted from all subsequent images.

Next, multiplicative noise, such as a CCD's pixel-to-pixel response, should be accounted for. This pixel-to-pixel response should be uniform across the image and to achieve this an average response may be divided out. The average response is referred to as a 'flat' image or flat-field and may be acquired by observing a uniformly illuminated region to determine the pixel-to-pixel response.

Night sky flats are produced from science images where the images contain mostly sky and are used in photometry. The science images are combined using the mode statistic which removes any celestial objects at the cost of a low Signal-to-Noise Ratio (S/N) flat-field. Twilight flats are produced from images of the twilight (or dawn) sky and are again used in photometry. They are taken when the Sun has just set, opposite the direction of the Sun at about 20° from zenith. Although these flats provide better S/Ns, careful planning is required as the sky's brightness changes rapidly. Finally, dome flats are images taken of a flat surface inside the telescopes dome and are used in both photometry and spectroscopy. The dome is uniformly and indirectly illuminated which allows for precise control of the light source.

A flat-field must be normalized before being used to correct any science images since it only acts to account for the pixel-to-pixel response and not for the additive errors. A normalized spectroscopic flat image, $F_\lambda^n(x, y)$, can be calculated as:

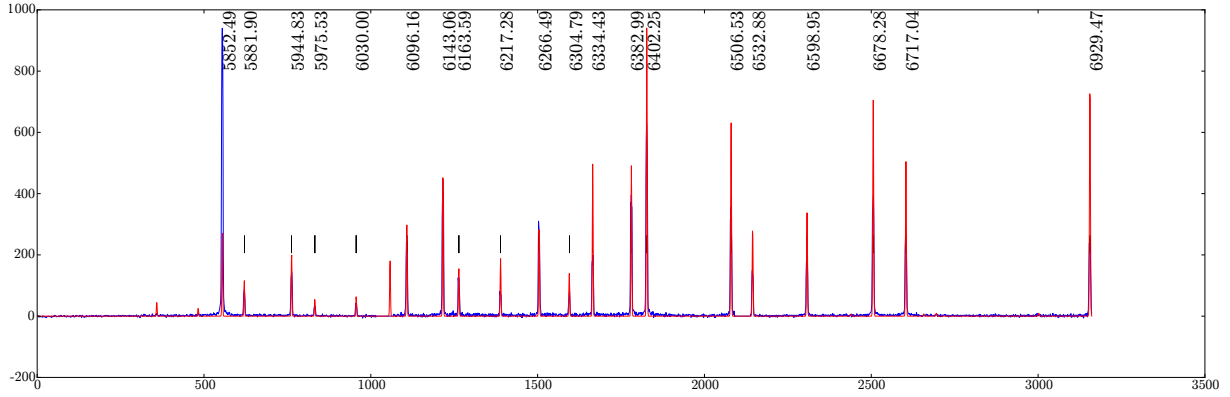


Figure 2.7: Example of an arc spectrum for NeAr taken with SALT’s RSS using the PG1800 grating at a grating angle of 34.625° , an articulation angle of 69.258° , and covering a wavelength range of $\sim 5600 - 6900\text{\AA}$. Plot adapted from SALT’s published Longslit Line Atlases (as of 2023)²

$$F_\lambda^n(x, y) = \frac{F_\lambda(x, y) - B(x, y) - (\frac{t_S}{t_D})D(x, y)}{\text{median}_{lp}(F_\lambda(x, y) - B(x, y) - (\frac{t_S}{t_D})D(x, y))} \quad (2.10)$$

where $F_\lambda(x, y)$ is the non-corrected flat image, $B(x, y)$ is the bias image, $D(x, y)$ is the dark image which is scaled by the exposure time of the science image, t_S , and the dark image, t_D . median_{lp} is a low-pass median filter which smoothes out any rapid changes in the pixel-to-pixel response, removing the illumination contribution.

The calibrated science image, $S_\lambda^*(x, y)$, which accounts for the bias and dark currents as well as the flat fielding can then be calculated as:

$$S_\lambda^*(x, y) = \frac{S_\lambda(x, y) - B(x, y) - (\frac{t_S}{t_D})D(x, y)}{F_\lambda^n(x, y)}. \quad (2.11)$$

Multichannel CCDs are detectors that use either multiple CCDs or a CCD with multiple output amplifiers which can be read out through multiple channels at the same time, increasing the detectors size while keeping the readout time constant. These CCD setups need additional calibrations, specifically cross-talk corrections and mosaicking. Cross-talk noise refers to contamination that occurs during readout in one channel from another channel with a high signal and occurs because the signals can not be completely isolated from one another. Cross-talk corrections therefore account for this signal contamination between channels being read out at the same time (Freyhammer et al., 2001). Mosaicking is necessary for multichannel CCDs since the digitized signal read out from the detector has no reference of the physical location of the pixel it was detected at. Mosaicking therefore orients the data acquired from a multichannel detector correctly relatively to one another so that a single image is produced from the multiple channels read out from the detector.

Wavelength Calibration

Finally, calibrations unique to spectroscopy are the wavelength calibrations. Since the dispersion element breaks the incident light into its constituent wavelengths non-linearly, as discussed in § 2.1.7, the relation between the pixel on a detector and the wavelength of

²NeAr plot sourced from <https://astronomers.salt.ac.za/data/salt-longslit-line-atlas/>

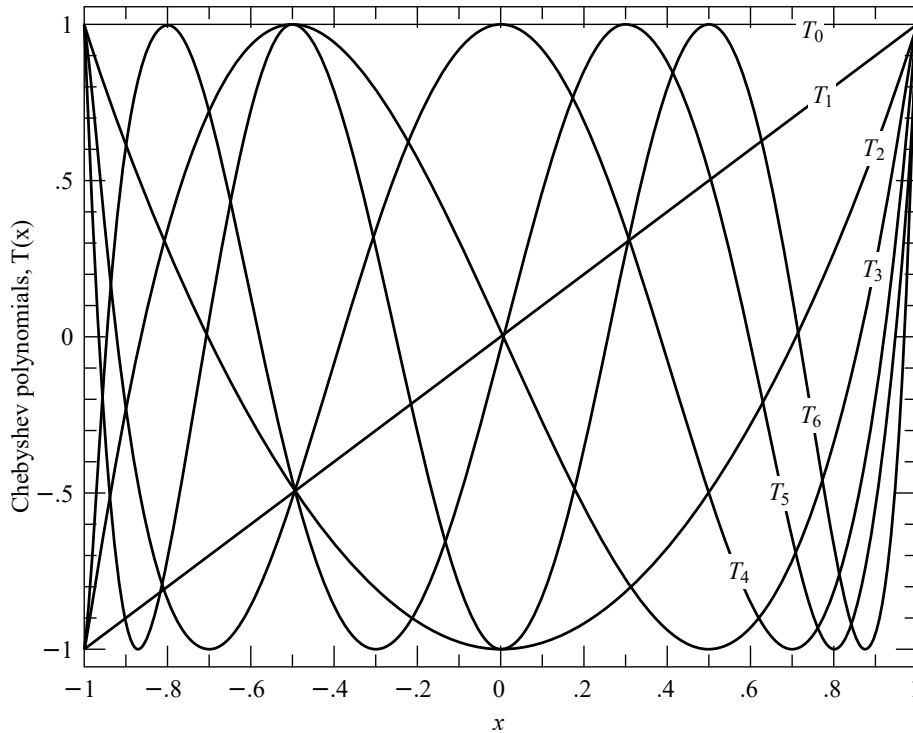


Figure 2.8: The first seven Chebyshev polynomials (T_0 through T_6) as defined by Equation 2.13 over the region $[-1, 1]$ for which they are orthogonal. Figure adapted from (Press et al., 2007) (2023)³

the light incident on it is unknown. Ideally, the spectrometer’s optics would be modeled to produce a reliable pixel to wavelength calibration (see E.g. Liu and Hennelly, 2022), but this becomes increasingly more difficult for spectrometers with complex, non-sedentary, optical paths. Alternatively, a source with well-defined spectral features, with said features evenly populating the wavelength region of interest, such as in Figure 2.7 may be observed. The observed frame is commonly referred to as an ‘arc’ frame, after the arc-lamps used to acquire the spectra, and should be observed alongside the science frames over the course of an observation run. It is important that the arc frame is observed at the same observing conditions and parameters as the science frames since the optical path will vary over the course of an observing run and for different observing parameters, invalidating previously acquired arc frames.

The wavelength calibrations then consist of defining a two-dimensional pixel-to-wavelength conversion function from the arc frame which may later be applied to calibrate the science frames. The two most common approximations for wavelength calibrations are the Chebyshev and Legendre polynomial approximations.

Chebyshev polynomials The Chebyshev polynomials are defined explicitly as:

$$T_n(x) = \cos(n \cos^{-1}(x)), \quad (2.12)$$

or recursively as:

$$\begin{aligned} T_0(x) &= 1 \\ T_1(x) &= x \\ T_n(x) &= 2xT_{n-1}(x) - T_{n-2}(x), \text{ for } n > 1 \end{aligned} \quad (2.13)$$

³Available digitally at numerical.recipes

where T is a Chebyshev polynomial⁴ of order n . An important property of Chebyshev polynomials is that they are orthogonal polynomials. This means that the inner product of any two differing Chebyshev polynomials, $T_i(x)$ and $T_j(x)$, over the range $[-1, 1]$ is zero, as shown by

$$\int_{-1}^1 T_i(x)T_j(x) \frac{1}{\sqrt{1-x^2}} dx = \begin{cases} 0, & i \neq j \\ \pi/2, & i = j \neq 0 \\ \pi, & i = j = 0 \end{cases} \quad (2.14)$$

where $1/\sqrt{1-x^2}$ is the weighting factor for Chebyshev polynomials. This property is important because it means that each coefficient in the Chebyshev polynomial expansion are independent of one another, allowing for a unique solution when approximating an unknown function.

An approximation, using Chebyshev polynomials, of an unknown wavelength calibration function is given by

$$f(x) \approx \sum_{i=0}^N c_i T_i(u) \quad (2.15)$$

or

$$F(x, y) \approx \sum_{i=0}^N \sum_{j=0}^M c_{ij} T_i(u) T_j(v), \quad (2.16)$$

for a one- or a two-dimensional wavelength surface function, respectively. Here N and M are the desired x and y orders, and c_i and c_{ij} are the Chebyshev polynomial coefficients (Florinsky and Pankratov, 2015; Leng, 1997). Since the orthogonality property of the Chebyshev polynomials only holds true over the range $[-1, 1]$, the $(x, y) \in ([0, a], [0, b])$ pixel coordinates must be remapped to $u, v \in [-1, 1]$ following the relation

$$(u, v) = \frac{2(x, y) - a - b}{b - a}. \quad (2.17)$$

The Chebyshev polynomials are more suited for wavelength calibrations than standard polynomials since they are orthogonal and have minima and maxima located at $[-1, 1]$, as seen in Figure 2.8. This means that the Chebyshev approximation is exact when $x = x_n$, where x_n are the positions of the $n - 1$ x -intercepts of $T_N(x)$. These properties greatly minimize the error in the Chebyshev approximation, even at lower order approximations (Arfken and Weber, 1999).

Legendre polynomials Similar to the Chebyshev polynomials, the Legendre polynomials may be defined explicitly as:

$$P_n(x) = \frac{1}{2^n n!} \frac{d^n}{dx^n} (x^2 - 1)^n \quad (2.18)$$

or recursively as:

⁴Denoted T as a hold-over from the alternate spelling, ‘Tchebycheff’.



Figure 2.9: The first six Legendre polynomials (P_0 through P_5) as defined by Equation 2.21 over the region $[-1, 1]$ for which they are orthogonal. Figure adapted from Geek3, CC BY-SA 3.0, via Wikimedia Commons (2023)

$$\begin{aligned}
 P_0(x) &= 1 \\
 P_1(x) &= x \\
 P_n(x) &= \frac{2n+1}{n+1}xP_{n-1}(x) - \frac{n}{n+1}P_{n-2}(x), \text{ for } n > 1
 \end{aligned} \tag{2.19}$$

where P is a Legendre polynomial of order n . Legendre polynomials also hold the property of orthogonality. This means that the inner product of any two differing Legendre polynomials, $P_i(x)$ and $P_j(x)$, over the range $[-1, 1]$ is zero, as shown by

$$\int_{-1}^1 P_i(x)P_j(x) dx = \begin{cases} 0, & i \neq j \\ \frac{2}{2n+1}, & i = j \end{cases} \tag{2.20}$$

where a weight of 1 is the weighting factor for Legendre polynomials.

An approximation, using Legendre polynomials, of an unknown wavelength calibration function is given by

$$f(x) \approx \sum_{n=0}^N a_n P_n(u) \tag{2.21}$$

or

$$F(x, y) \approx \sum_{i=0}^N \sum_{j=0}^M a_{ij} P_i(u) P_j(v), \tag{2.22}$$

for a one-dimensional wavelength function or a two-dimensional surface function, respectively. Here N and M are the desired x and y orders, u and v are the same mapping variable as in Equation 2.17, and a_{ij} are the Legendre polynomial coefficients.

Legendre polynomials benefit from having the orthogonality condition with no weight necessary ($w = 1$) which makes their coefficients computationally easier to compute but

increases the error in a Legendre approximation when compared to that of the error in a Chebyshev approximation for a function⁵ (Ismail, 2005).

Regardless of which method of polynomial approximation is chosen, the polynomials are fit by varying the relevant coefficients using the least squares method. The resultant minimized function may then be used to convert the science frames from an (x -pixel, y -pixel) coordinate system to a (λ , y -pixel) coordinate system.

2.2 Polarimetry

Both Huygens and Newton came to the conclusion that light demonstrates transversal properties (Huygens, 1690; Newton and Innys, 1730), which was later further investigated and coined as ‘polarization’ by Malus (Malus, 1809). Malus also investigated the polarization effects of multiple materials including some of which were birefringent, such as optical calcite, which he referred to as Iceland spar after Bartholinus’ investigations of the material (Bartholinus, 1670).

Fresnel built on Malus’ work showing that two beams of light, polarized at a right angle to one another, do not interfere, conclusively proving that light is transversal in nature, opposing the widely accepted longitudinal nature of light due to the prevalent belief in the ether. Fresnel later went on to correctly describe how polarized light is reflected and refracted at the surface of optical dielectric interfaces, without knowledge of the electromagnetic nature of light. Fresnel’s equations for the reflectance and transmittance, R and T , are defined as:

$$\begin{aligned} R_s &= \left| \frac{Z_2 \cos \theta_i - Z_1 \cos \theta_t}{Z_2 \cos \theta_i + Z_1 \cos \theta_t} \right|^2 \\ R_p &= \left| \frac{Z_2 \cos \theta_t - Z_1 \cos \theta_i}{Z_2 \cos \theta_t + Z_1 \cos \theta_i} \right|^2 \\ T_s &= 1 - R_s \\ T_p &= 1 - R_p \end{aligned} \tag{2.23}$$

where s and p are the two polarized components of light perpendicular to one another, Z_1 and Z_2 are the impedance of the two media, and θ_i , θ_t , and θ_r are the angles of incidence, transmission, and reflection, respectively (Fresnel, 1870).

Nicol was the first to create a polarizer, aptly named the Nicol prism, where the incident light is split into its two perpendicular polarization components, namely the ordinary and extraordinary beams. Faraday discovered the phenomenon where the polarization plane of light is rotated when under the influence of a magnetic field, known as the Faraday effect. Brewster calculated the angle of incidence, θ_B , at which incident polarized light is perfectly transmitted through a transparent surface, with refractive indexes of n_1 and n_2 , while non-polarized incident light is perfectly polarized when reflected and partially polarized when refracted.

$$\theta_B = \arctan \frac{n_2}{n_1} \tag{2.24}$$

⁵For one-dimensional Legendre and Chebyshev approximations of the same order, N



Figure 2.10: Nicol prism diagram for incident non-polarized light.

Stokes' work created the first consistent description of polarization and gave us the Stokes parameters which give an operational approach to polarization, discussed later in more detail (Stokes, 1851). Hale was the first to apply polarization to astronomical observations, using a Fresnel rhomb and Nicol prism as a quarter-wave plate and polarizer, respectively (Hale, 1908, 1979). Wollaston also created a prism, similarly named the Wollaston prism, which allowed simultaneous observation of the ordinary and extraordinary beams due to the smaller deviation angle (Wollaston, 1802). Finally, Chandrasekhar's work furthered our understanding of astrophysical polarimetry by explaining the origin of polarization observed in starlight as well as mathematically modeling the polarization of rotating stars, which came to be named Chandrasekhar polarization (Chandrasekhar, 1950).

2.2.1 Polarization

Maxwell's equations for an electromagnetic field propagating through a vacuum are given as:

$$\begin{aligned}\nabla \cdot \mathbf{E} &= 0 \\ \nabla \cdot \mathbf{B} &= 0 \\ \nabla \times \mathbf{E} &= -\frac{1}{c} \frac{\partial \mathbf{B}}{\partial t} \\ \nabla \times \mathbf{B} &= \frac{1}{c} \frac{\partial \mathbf{E}}{\partial t}\end{aligned}\tag{2.25}$$

where \mathbf{E} and \mathbf{B} are the electric and magnetic field vectors, and c is the speed of light (Griffiths, 2005). In a right-handed (x, y, z) coordinate system, a non-trivial solution of an electromagnetic wave following Maxwell's Equations propagating along the z -axis, towards a hypothetical observer, is described by:

$$\mathbf{E} = E_x \cos(\omega t - \Phi_x) \hat{\mathbf{x}} + E_y \cos(\omega t - \Phi_y) \hat{\mathbf{y}}\tag{2.26}$$

where E_x , E_y , Φ_x , and Φ_y are all parameters describing the amplitude and phase of the electric field vector in the (x, y) plane. Rewriting Equation 2.26 using complex values allows us to simplify the form of the solution to:

$$\mathbf{E} = \Re(\mathbf{E}_0 e^{-i\omega t})\tag{2.27}$$

where we only consider the real part of the equation, and where \mathbf{E}_0 is defined as:

$$\mathbf{E}_0 = E_x e^{i\Phi_x} \hat{\mathbf{x}} + E_y e^{i\Phi_y} \hat{\mathbf{y}}\tag{2.28}$$

and is referred to as the polarization vector since it neatly contains the parameters responsible for the polarization properties (Degl'Innocenti, 2014).



Figure 2.11: The polarization ellipse for an electric field vector propagating through free space.

For an electric field vector with oscillations in some combination of the x and y axes, the tip of the vector sweeps out an ellipse, as depicted in Figure 2.11. This ellipse is referred to as the polarization ellipse and has the form:

$$\left(\frac{\mathbf{E}_x}{\mathbf{E}_{0,x}}\right)^2 + \left(\frac{\mathbf{E}_y}{\mathbf{E}_{0,y}}\right)^2 - \frac{2\mathbf{E}_x\mathbf{E}_y}{\mathbf{E}_{0,x}\mathbf{E}_{0,y}} \cos \Phi = \sin^2 \Phi \quad (2.29)$$

where $\Phi = \Phi_x - \Phi_y$ and is the phase difference between the x and y phase parameters. The degree of polarization for the polarization ellipse is related to the eccentricity of the ellipse and the angle at which it is rotated relates to the polarization angle. Since $\mathbf{E}_{0,x}$, $\mathbf{E}_{0,y}$, Φ_x , and Φ_y describe the wave, the polarization ellipse that results from these parameters is fixed as the wave continues to propagate. An alternate representation of Equation 2.29 is given by:

$$(E_x^2 + E_y^2)^2 - (E_x^2 - E_y^2)^2 - (2E_x E_y \cos \Phi)^2 = (2E_x E_y \sin \Phi)^2 \quad (2.30)$$

where

$$\begin{aligned} P_I &= E_x^2 + E_y^2, \\ P_Q &= E_x^2 - E_y^2, \\ P_U &= 2E_x E_y \cos \Phi, \text{ and} \\ P_V &= 2E_x E_y \sin \Phi. \end{aligned} \quad (2.31)$$

From Equations 2.30, 2.31, the polarization parameters are related by:

$$P_I^2 = P_Q^2 + P_U^2 + P_V^2. \quad (2.32)$$

There is, however, a seemingly small albeit major shortcoming of the polarization as defined in Equation 2.31, the polarization ellipse as represented by Figure 2.11 deals only with a single transverse wave and is incapable of handling a wave-packet made up of multiple waves. This is because the waves making up a wave-packet will not share their polarization properties and will temporally vary from one another. By taking the time average of the waves in a wave-packet, which happens inherently in the process of observations, this temporal variation may be eliminated.

$$\langle \mathbf{E}_i \mathbf{E}_j \rangle = \lim_{dt \rightarrow \infty} \frac{1}{T} \int_0^T \mathbf{E}_i \mathbf{E}_j dt, \text{ for } i, j \in (x, y) \quad (2.33)$$

where T is the total averaging time over electric field vectors \mathbf{E}_i and \mathbf{E}_j . Equation 2.31 now simplifies to:

$$\mathbf{S} = \begin{pmatrix} S_0 \\ S_1 \\ S_2 \\ S_3 \end{pmatrix} = \begin{pmatrix} I \\ Q \\ U \\ V \end{pmatrix} = \begin{pmatrix} \langle E_x^2 + E_y^2 \rangle \\ \langle E_x^2 - E_y^2 \rangle \\ \langle 2E_x E_y \cos \Phi \rangle \\ \langle 2E_x E_y \sin \Phi \rangle \end{pmatrix} \quad (2.34)$$

where $S_0 - S_3$ are referred to as the Stokes (polarization) parameters (Stokes, 1851).

Only beams of completely polarized light could be accounted for before Stokes' work polarization. For a reference direction which defines the direction of the x -axis of our coordinate system, the Stokes parameters are physically described as follows: the Q parameter is defined as the difference between the amount of photons oscillating parallel and perpendicular to the reference direction, the U parameter is defined as the difference between the amount of photons oscillating at 45° and 135° counter-clockwise from the reference direction, and the V parameter is defined as the difference between the amount of photons with right-handed (positive, clockwise) circular polarization and left-handed (negative, counter-clockwise) circular polarization (Stokes, 1851).

Using the Stokes parameters, we can now account for partially polarized light such that:

$$I^2 \geq Q^2 + U^2 + V^2, \quad (2.35)$$

where it should be noted that (I, Q, U, V) represent the partial polarization parameters and are related to (P_I, P_Q, P_U, P_V) since the polarization may be partial. In general, and henceforth, (P_I, P_Q, P_U, P_V) are relative quantities normalized to the intensity, where

$$P_I = 1, \quad P_Q = \frac{Q}{I}, \quad P_U = \frac{U}{I}, \text{ and } P_V = \frac{V}{I}. \quad (2.36)$$

Similar to the polarization ellipse, the Stokes parameters may be depicted using the Poincaré sphere in spherical coordinates $(IP, 2\Psi, 2\chi)$, where I denotes the total intensity and P the degree of polarization, or the ratio of polarized to non-polarized light in the wave-packet, χ denotes the polarization angle, and Ψ denotes the ellipticity angle of the polarization ellipse. It should be noted that the Poincaré sphere also uses the normalized Stokes parameters ($S_0 = 1$) as defined above in equation 2.36.

$$\begin{aligned} I &= S_0 \\ P &= \frac{\sqrt{S_1^2 + S_2^2 + S_3^2}}{S_0}, \text{ for } 0 \leq P \leq 1 \\ 2\Psi &= \arctan \frac{S_3}{\sqrt{S_1^2 + S_2^2}} \\ 2\chi &= \arctan \frac{S_2}{S_1} \end{aligned} \quad (2.37)$$

2.2.2 Polarization Measurement

Except for polarimetry in the radio-wavelength regime, the polarization of a beam can not be directly measured. The polarization properties may, however, be recovered from

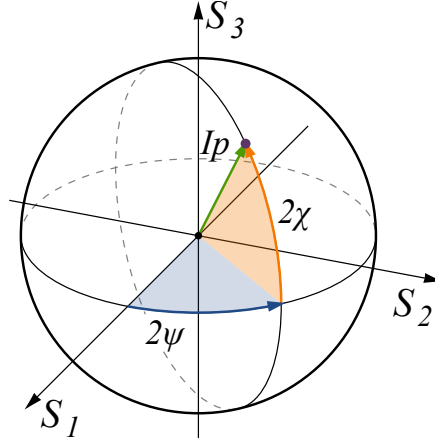


Figure 2.12: The Poincaré sphere describing the polarization properties of a wave-packet propagating through free space. Figure adapted from Wikimedia Commons (2023)

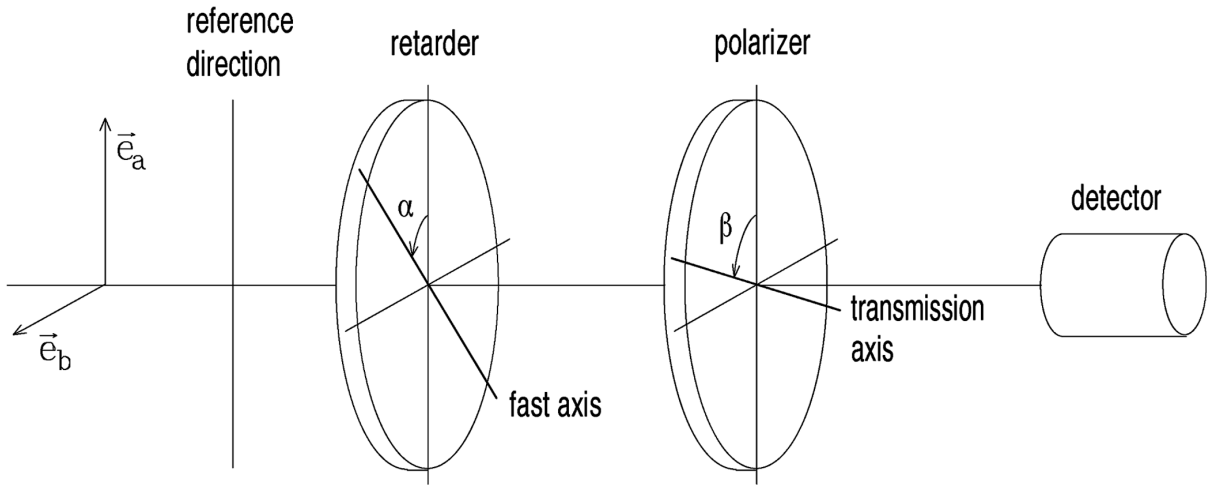


Figure 2.13: Diagram of an ideal polarimeter. Figure adapted from Degl’Innocenti and Landolfi (2004).

the beam through manipulation of the four parameters mentioned in Equation 2.26. This so-called manipulation is achieved by passing the beam through optical elements which vary the beam for differing amplitudes and phases. These matrix operations may be represented by their corresponding Mueller matrices. For ideal components, the resultant beam \mathbf{S}' after passing through an optical element is given by

$$\mathbf{S}' = \mathbf{M}\mathbf{S} \quad (2.38)$$

where \mathbf{S} is the beam incident on the optical element and \mathbf{M} represents the 4×4 Mueller matrix representing the optical element. Mueller matrices are especially useful when dealing with paths through optical elements as they observe the ‘train’ property (Priebe, 1969). This means that an incoming beam \mathbf{S} passing, in order, through elements with known Mueller matrices $(\mathbf{M}_0, \dots, \mathbf{M}_N)$ results in an outgoing beam \mathbf{S}' such that:

$$\mathbf{S}' = \mathbf{M}_N \dots \mathbf{M}_0 \mathbf{S} \quad (2.39)$$

Some Mueller Matrices are given below with angles related to those in Figure 2.13, measured counter-clockwise in a right-handed coordinate system.

General rotation The Mueller matrix for coordinate space rotations about the origin by an angle θ .

$$\mathbf{R}(\theta) = \begin{bmatrix} 1 & 0 & 0 & 0 \\ 0 & \cos 2\theta & \sin 2\theta & 0 \\ 0 & -\sin 2\theta & \cos 2\theta & 0 \\ 0 & 0 & 0 & 1 \end{bmatrix} \quad (2.40)$$

General linear retardance The Mueller matrix for retardance where α is the angle between the incoming vector and fast axis, and δ is the retardance introduced by the retarder. The retarder is often referred to by this retardance, e.g. if the retardance is $\delta = \pi$ or $\pi/2$, the retarder is referred to as a half- or quarter-wave plate, respectively.

$$\mathbf{W}(\alpha, \delta) = \begin{bmatrix} 1 & 0 & 0 & 0 \\ 0 & \cos^2 2\alpha + \sin^2 2\alpha \cos \delta & \cos 2\alpha \sin 2\alpha (1 - \cos \delta) & \sin 2\alpha \sin \delta \\ 0 & \cos 2\alpha \sin 2\alpha (1 - \cos \delta) & \cos^2 2\alpha \cos \delta + \sin^2 2\alpha & -\cos 2\alpha \sin \delta \\ 0 & -\sin 2\alpha \sin \delta & \cos 2\alpha \sin \delta & \cos \delta \end{bmatrix} \quad (2.41)$$

General linear polarization The Mueller matrix for linear polarization where β is the angle between the incoming vector and transmission axis.

$$\mathbf{P}(\beta) = \frac{1}{2} \begin{bmatrix} 1 & \cos 2\beta & \sin 2\beta & 0 \\ \cos 2\beta & \cos^2 2\beta & \cos 2\beta \sin 2\beta & 0 \\ \sin 2\beta & \sin 2\beta \cos 2\beta & \sin^2 2\beta & 0 \\ 0 & 0 & 0 & 0 \end{bmatrix} \quad (2.42)$$

These matrices in combination with Equation 2.39 allow us to describe how the Stokes parameters would change when passing through various optical elements. For a setup similar to Figure 2.13, we can vary the retardance angle, α , and polarization angle, β , for a wave plate with a relative phase difference, γ , to acquire a system of equations that we can solve to retrieve the Stokes polarization parameters (Bagnulo et al., 2009).

$$\begin{aligned} S(\alpha, \beta, \gamma) \propto \frac{1}{2} \{ & I + [Q \cos 2\alpha + U \sin 2\alpha] \cos(2\beta - 2\alpha) \\ & - [Q \sin 2\alpha + U \cos 2\alpha] \sin(2\beta - 2\alpha) \cos \gamma \\ & + V \sin(2\beta - 2\alpha) \sin \gamma \} \end{aligned} \quad (2.43)$$

Several or more frames taken under differing configurations may be used to reduce a system of equations to extract all four Stokes polarization parameters, but it is possible to extract the I , Q and U polarization parameters using only four frames, or two dual-beam frames, for well-chosen configurations and assuming ideal components. This ideal configuration varies the retarder angle such that $\Delta\alpha = \pi/8$ while keeping the polarizer stationary. More frames for additional retarder angles are advisable and often necessary, however, as they correct for any differences in sensitivity, such as may arise in a polarized flat field and which is further discussed in § 2.2.3 (Patat and Romaniello, 2006).

From Equation 2.43 we see that the linear retarder element is the driving element of a polarizer as the first three Stokes parameters (S_{0-2} , or I , Q , and U) may be found by changing only the angle of retardance, α .

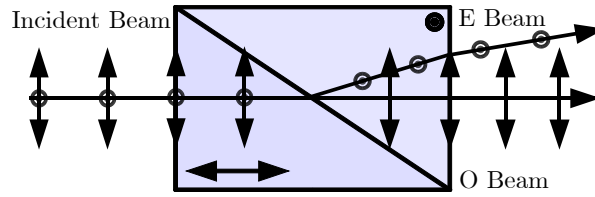


Figure 2.14: Diagram of a Rochon prism. Figure adapted from Wikimedia Commons (2023)

Wave plates Wave plates, also commonly referred to as retarders, are generally made from optically transparent birefringent crystals. A wave plate has a fast and slow axis, which are perpendicular to one another and both perpendicular to an incident beam. Due to the birefringence of the wave plate medium, the phase velocity of the beam polarized parallel to the fast axis, namely the extraordinary beam, slightly increases while that of the beam polarized parallel to the slow axis, namely the ordinary beam, remains unaffected (Hecht, 2017).

This difference in the perpendicular component's phase velocities introduces a relative phase difference between the two beams, γ , which is given by:

$$\gamma = \frac{2\pi\Delta n L}{\lambda_0} \quad (2.44)$$

where Δn and L refer to the birefringence and thickness of the wave plate medium, respectively, and λ_0 refers to the vacuum wavelength of the beam.

This relative phase difference determines the name of the wave plate, such as the half- and quarter-wave plates referring to the $\gamma = m(\pi/2)$ and $\gamma = m(\pi/4)$ for $m \in \mathbb{Z}^+$, respectively, which are also the most commonly used wave plates. Phase differences with an integer multiple of one another still relate to the same phase difference and are referred to as multiple-order wave plates. Multiple multiple-order wave plates can be combined by alternatively aligning the fast axis of one to the slow axis of another to create a compound zero-order wave plate. When the phase difference of the wave plate is not an integer difference it is referred to as a zero-order wave plate (Hale and Day, 1988).

Polarizers Polarizers are typically made from two prisms, of a birefringent material, cemented together with an optically transparent adhesive. The actual effect of separating the perpendicular polarization components is achieved using varying effects, namely through:

- absorption of one of the polarized components, such as in Polaroid polarizing filters,
- total internal reflection of a single polarized component, such as in a Nicol prism (Figure 2.10),
- Refraction of a single polarized component, such as in a Rochon prism (Figure 2.14), or
- Refraction of both polarization components in differing directions, such as in a Wollaston prism (Figure 2.15).

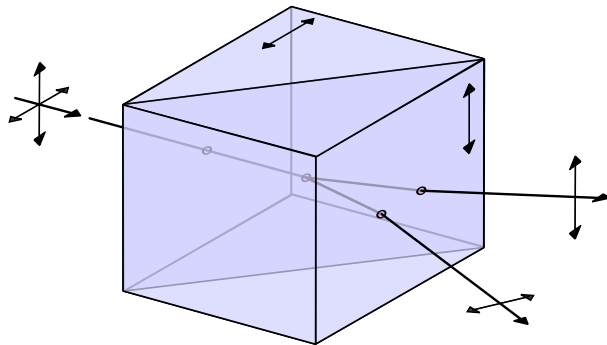


Figure 2.15: Diagram of a Wollaston prism. Figure adapted from Wikimedia Commons (2023)

Wollaston prisms The Wollaston prism consists of two prisms consisting of a birefringent monoaxial material, cemented together with an optically transparent adhesive along their hypotenuses with their optical axes orthogonal, as seen in Figure 2.15. The Wollaston prism is a common optical polarizing element in astrophysical polarimetry which separates an incident beam into two linearly polarized beams, orthogonal to one another, as expected of a polarizer, but which returns the two beams deviated from their common axis equally. The deviation angle is determined by the right-angle prism base angles (Simon, 1986).

Wollaston prisms are beneficial over simpler elements, as listed previously, since a single frame allows for the observation of a set of orthogonal polarization configurations. This halves the observational time required to collect enough data to calculate the Stokes parameters, at the cost of an increase in calibration and reduction difficulty.

2.2.3 Polarimetric calibrations

Detector Calibrations

Similar to § 2.1.8, polarimetric calibrations are necessary when dealing with a polarimeter, though as the optical elements differ the calibrations also differ. Corrections and calibrations related to the CCD remain unchanged while those related to correcting for the optical elements only need to be modified to correct for polarization instead of wavelength.

Flat Fielding

Once the CCD calibrations have been completed, the polarization intrinsic to the optical elements needs to be accounted for such that the pixel-to-pixel response is made uniform. Flat-fielding can once again be used to correct for this. The flats taken for polarimetry, however, introduce an additional challenge as the targets for conventional flats are polarized, such as twilight and dome flats which are polarized by light scattering in the atmosphere and the reflective surface of the dome, respectively.

If no unpolarized flat images can be taken for flat field calibrations then, when possible due to the polarimeter design, the wave plate may be constantly rotated to act as a depolarizing element and is effective so long as the wave plate is rotated faster than the flat's exposure time. Alternatively, spatially constant polarized flats may be used with

the added restriction that additional exposures for the science and flat images are taken. Redundant exposures are simply exposures taken with a half-wave plate angle that differs from an existing exposure by $\pi/4$. The introduced redundancy partially cancels out any uniform polarization across beams and more redundant observations allow for an increased cancellation efficiency. Increasing the amount of redundant observations also increases the time needed to observe all the exposures, which in turn introduces time-dependent effects such as fringing or intensity variations of the source. As such, a balance must be found for the amount of redundant frames observed. In any case, when the flat contains any polarization, the removal of the uniform polarization from the science frames is left for when the polarization is calculated (Patat and Romaniello, 2006; Peinado et al., 2010).

Dual-beam Extraction and Alignment

After calibrations for the CCD and light path are accounted for, the *O*- and *E*-beams can be extracted and further reduced. The extraction depends heavily on the layout of the polarimeter but often a simple cropping of the differing sections is enough to separate the two images.

The matching dual images need to be aligned once they have been extracted such that the sources present in them overlap. The Wollaston prism needs to be corrected for as it introduces a Wollaston prism beam deviation. The aligning of the *O*- and *E*-beams is crucial as the comparison of the dual images is what allows for the calculation of the polarization properties.

Sky Subtraction

The polarization introduced by the sky needs to be removed as it will influence the polarization results of the target source. Thankfully, the background polarization is an additive type of noise and may be subtracted out across the frames. This subtraction should be done for each beam in each frame, however, as the background intensity of each image will differ as the background polarization differs.

2.3 Spectropolarimetry

As the name suggests, spectropolarimetry is the measurement of the polarization of light for a chosen spectral range and provides polarimetric results as a function of wavelength. The history of spectropolarimetry is defined by the advancements of spectrometers and polarimeters, given in § 2.2, 2.1. The most notable historical contributions unrelated to spectroscopy or polarimetry, however, are those of spectropolarimetric studies instead of instrumental developments.

Spectropolarimetry can provide further insights into a materials physical structure, chemical composition, and magnetic field, allowing spectropolarimetry to be useful across multiple disciplines. In astronomy in particular, spectropolarimetry has been used to study the magnetic field, chemical composition, and underlying structure and emission processes of multiple types of celestial objects (see for example Antonucci and Miller, 1985; Donati et al., 1997; Wang and Wheeler, 2008).

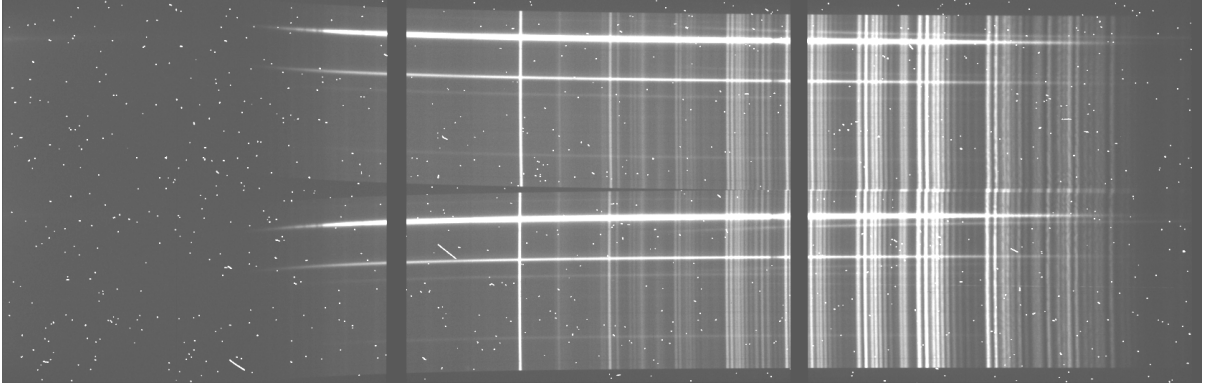


Figure 2.16: A spectropolarimetric target exposure as observed by the SALT RSS in spectropolarimetry mode.

Along with common points of consideration when developing any instrumentation for observational astronomy, such as resolution and sensitivity, spectropolarimeters need to consider the spectral response of the polarimetric components as well as the polarization response of the spectroscopic components as both are simultaneously in the light-path during observations and have noticeable affects on one another. Time is another constraint for spectropolarimetry as the incident light is separated both by wavelength and by polarization states. This division of the incident light results in increased exposure times of not only observations of targets but also observations needed for calibrations, both of which are time-dependent.

Figure 2.16 illustrates a typical science image taken with a spectropolarimeter. The image contains the O - and E -beams which are both dispersed into their spectra. Spectropolarimetric results are acquired from measurements and calibrations of these images alongside any necessary calibration images.

2.3.1 Spectropolarimetric measurement

The derived relations given in § 2.2.1, such as the Stokes parameters, are valid for both polarimetry and spectropolarimetry due to the time averaging, which accounts for temporal variations and permits partially polarized incident beams, and the achromatic nature of the polarization calculations.

For linear spectropolarimetry with half-wave plate angles of θ_i , an exposure measures the wavelength dependent intensities of the O - and E -beams, $I'_O(\lambda)$ and $I'_E(\lambda)$, respectively. The O - and E -beam intensities thus relate to the Stokes parameters following:

$$\begin{aligned} I'_{O,i}(\lambda) &= \frac{1}{2}[I + Q \cos(4\theta_i) + U \sin(4\theta_i)], \\ I'_{E,i}(\lambda) &= \frac{1}{2}[I - Q \cos(4\theta_i) - U \sin(4\theta_i)]. \end{aligned} \quad (2.45)$$

At least two exposures are needed to solve for the I , Q , and U polarization parameters since two equations arise from a single exposure of a dual-beam configuration and at least four linear equations are required to solve for three variables in a system of linear equations.

The first Stokes parameter, I , may be recovered for each dual-beam exposure as

$$I(\lambda) = f_{O,i}(\lambda) + f_{E,i}(\lambda). \quad (2.46)$$

Next, the second and third Stokes parameters, Q and U , are found by first defining the normalized difference in relative intensities as

$$F_i(\lambda) \equiv \frac{f_{O,i}(\lambda) - f_{E,i}(\lambda)}{f_{O,i}(\lambda) + f_{E,i}(\lambda)} \quad (2.47)$$

which then allows Equation 2.45 to be written in terms of the normalized Stokes parameters, $\bar{Q} = Q/I$ and $\bar{U} = U/I$, or, alternatively, the degree of polarization, P , and polarization angle, χ :

$$F_i(\lambda) = \bar{Q}(\lambda) \cos(4\theta_i) + \bar{U}(\lambda) \sin(4\theta_i) = P \cos(4\theta_i - 2\chi). \quad (2.48)$$

The optimal change in waveplate angle is $\Delta\theta = \pi/8$ as it allows the normalized Stokes polarization parameters to be written as:

$$\begin{aligned} \bar{Q}(\lambda) &= \frac{2}{N} \sum_{i=0}^{N-1} F_i(\lambda) \cos\left(\frac{\pi}{2}i\right) \\ \bar{U}(\lambda) &= \frac{2}{N} \sum_{i=0}^{N-1} F_i(\lambda) \sin\left(\frac{\pi}{2}i\right) \end{aligned} \quad (2.49)$$

where N is the amount of exposures taken, limited such that $N \in [2, 16]$, and F_i is the normalized difference in relative intensities for the i^{th} exposure (Patat and Romaniello, 2006).

The desired degree of polarization as well as the polarization angle for linear spectropolarimetry is calculated as:

$$\begin{aligned} P &= \sqrt{\bar{Q}^2 + \bar{U}^2} \\ \chi &= \frac{1}{2} \arctan \frac{\bar{U}}{\bar{Q}} \end{aligned} \quad (2.50)$$

which is derived from Equations 2.37 or by solving a system of linear equations of Equation 2.48 (Degl'Innocenti et al., 2006; Keller, 2002).

2.3.2 Spectropolarimetric calibrations

The calibrations necessary for the measurement to take place are, as always, seemingly more involved than the calculation of the results themselves. As spectropolarimetry is an amalgamation of spectroscopy and polarimetry, it naturally follows that the calibrations necessary are a combination of both calibrations, as discussed in § 2.1.8, 2.2.3. Even though the spectrometer and polarizer components both have an effect on an incident beam following the light-path through the spectropolarimeter, the calibrations procedures for both components remain mostly independent of one another and as such need not be repeated here.

Spectropolarimetric calibrations are, however, more involved when compared to the previous calibration discussions as minor deviations in the calibrations across the spectra

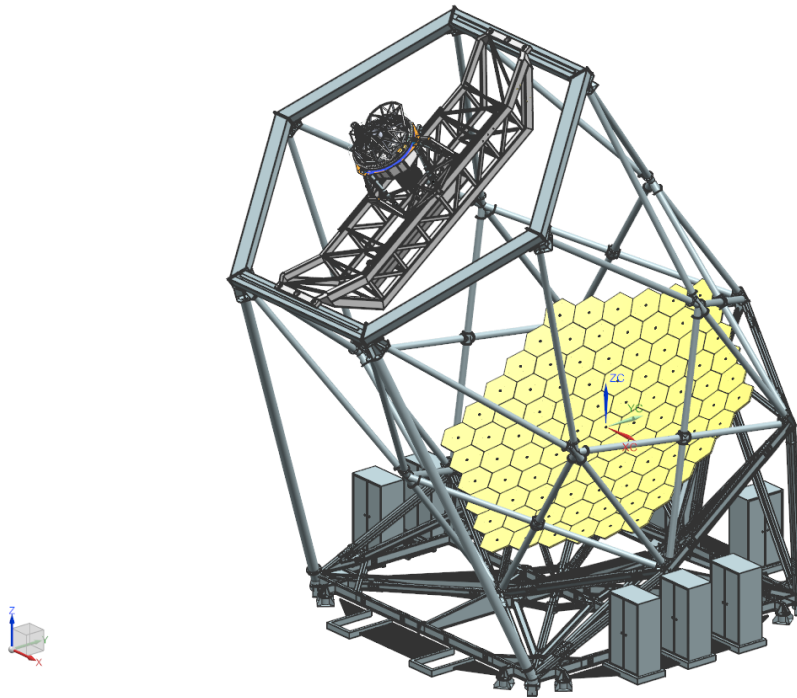


Figure 2.17: The tracker, supporting structure, and primary mirror of SALT. Figure adapted from the SALT call for proposals (2022)⁶

and the polarized beam may compound, resulting in poor S/N's for the spectropolarimetric results. Generally, more exposures over longer timespans are required to acquire enough redundancy and signal for the calculation of the Stokes parameters on top of the time necessary for calibrations to be completed. It should therefore be noted just how important the wavelength and image alignment calibrations are when dealing with spectropolarimetry.

2.4 The Southern African Large Telescope

SALT is a 10 m class optical/near-infrared telescope situated at the South African Astronomical Observatory (SAAO) field station near Sutherland, South Africa (Burgh et al., 2003). The operational design was based off of the Hobby-Eberly Telescope (HET) situated at McDonald Observatory, Texas, which limits the pointing of the telescope's primary mirror to a fixed elevation (37° from zenith in the case of SALT) while still allowing for full azimuthal rotation (Ramsey et al., 1998). Both SALT and HET utilize a spherical primary mirror which is stationary during observations and a tracker housing most of the instrumentation that tracks the primary mirrors spherically shaped focal path. Figure 2.17 depicts SALT's tracker (top left), supporting structure, and primary mirror (bottom right).

2.4.1 The primary mirror

The primary mirror is composed of 91 individual 1 m hexagonal mirrors which together form an 11 m segmented spherical mirror. Each mirror segment can be adjusted by

⁶http://pysalt.salt.ac.za/proposal_calls/current/ProposalCall1.html



Figure 2.18: The visibility annulus of objects observable by SALT. Figure adapted from the SALT call for proposals (2013)⁷

actuators allowing the individual mirrors to approximate a single monolithic spherical mirror. The fixed elevation means that SALT’s primary mirror has a fixed gravity vector allowing for a lighter, cost-effective supporting structure when compared to those of a more traditional altitude-azimuthal mount but with the trade-off that the control mechanism and tracking has increased complexity (Buckley et al., 2006).

2.4.2 Tracker and tracking

During observations the primary mirror is stationary and the tracker tracks celestial objects across the sky by moving along the primary focus. The tracker is capable of 6 degrees of freedom with an accuracy of $5 \mu\text{m}$ and is capable of tracking $\pm 6^\circ$ from the optimal central track position. Targets at declinations from 10.5° to -75.3° , as shown in Figure 2.18 are accessible during windows of opportunity. As the tracker moves along the track the effective collecting area varies and thus SALT has a varying effective diameter of $\sim 7 \text{ m}$ to 9 m when the tracker is furthest and closest to the optimal central position, respectively.

The tracker is equipped with a 4 mirror spherical aberration corrector (O’Donoghue,

⁷https://pysalt.salt.ac.za/proposal_calls/2013-2/



Figure 2.19: The optical path of the SALT RSS. Figure adapted from the SALT call for proposals (2023)⁸

2000), and an atmospheric dispersion compensator (O'Donoghue, 2002), which corrects for the spherical aberration caused by the geometry of the primary mirror and allows access to wavelengths as short as 3200 Å. These return a corrected flat focal plane with an 8' diameter field of view at prime focus on to the science instruments, with a 1' annulus around it used by the Tracker in a closed-loop guidance system.

2.4.3 SALT Instrumentation

SALT is equipped with the SALT Imaging Camera (SALTICAM) and the RSS science instruments onboard the tracker, and the High Resolution Spectrograph (HRS) and Near Infra-Red Washburn Labs Spectrograph (NIRWALS) science instruments which are fibre-fed from the tracker to their own climate controlled rooms. The RSS is currently the most used instrument on SALT and the only instrument used for spectropolarimetry.

NIRWALS

The NIRWALS is currently being commissioned and will have a wavelength coverage of 8000 to 17000 Å, providing medium resolution spectroscopy at $R = 2000$ to 5000 over Near Infra-Red (NIR) wavelengths (Brink et al., 2022; Wolf et al., 2022). This is ideally suited for studies of nearby galaxies.

HRS

The HRS echelle spectrograph was designed for high resolution spectroscopy at $R = 37000 - 67000$ covering a wavelength range of 3700 - 8900 Å and consists of a dichroic beam splitter and two VPH gratings (Nordsieck et al., 2003). This instrument is capable of stellar atmospheric and radial velocity analysis.

⁸https://pysalt.salt.ac.za/proposal_calls/current/ProposalCall.html

Grating Name	Wavelength Coverage (Å)	Usable Angles (°)	Bandpass per tilt (Å)	Resolving Power (1.25" slit)
PG0300 ⁹	3700 – 9000		3900/4400	250 – 600
PG0700 ⁹	3200 – 9000	3.0 – 7.5	4000 – 3200	400 – 1200
PG0900	3200 – 9000	12 – 20	~ 3000	600 – 2000
PG1300	3900 – 9000	19 – 32	~ 2000	1000 – 3200
PG1800	4500 – 9000	28.5 – 50	1500 – 1000	2000 – 5500
PG2300	3800 – 7000	30.5 – 50	1000 – 800	2200 – 5500
PG3000	3200 – 5400	32 – 50	800 – 600	2200 – 5500

Table 2.1: Gratings available for use with the RSS. Table adapted from the SALT call for proposals (2023).

SALTICAM

The SALTICAM functions as the acquisition camera and simple science imager with various imaging modes, such as full-mode and slot-mode imaging, and supports low exposure times, down to 50 ms (O’Donoghue et al., 2006). This enables photometry of faint objects, especially at fast exposure times.

RSS

The RSS functions as the primary spectrograph on SALT and can operate in long-slit spectroscopy and spectropolarimetry modes, a narrowband imaging mode, and multi-object and high resolution spectroscopy modes (for an in-depth discussion on operational modes see Kobulnicky et al., 2003, or the latest call for proposals).

The Detector The RSS detector consists of a mosaic of 3 CCD chips with a total pixel scale of 0.1267" per unbinned pixel with varying readout times depending on the binning and readout mode. The mosaicking results in a characteristic double ‘gap’ in the frames and resultant spectra taken with the RSS, as seen in Figure 2.16.

The Available Gratings The RSS is equipped with a rotatable magazine of six VPH gratings, as listed in Table 2.1. Observations may be planned using simulator tools provided by SALT and are performed in the first order only. The RSS has a clear filter, as well as three Ultraviolet (UV) (with differing lower filtering ranges) and one blue order blocking filter available, used in conjunction with the various gratings to block out contamination from the second order.

2.5 RSS Spectropolarimetry

Spectropolarimetry using the RSS is currently commissioned for long-slit linear spectropolarimetry, (I, Q, U) , where observations are taken following the waveplate pattern lists as in Table 2.2. Circular, (I, V) , and all-Stokes, (I, Q, U, V) , spectropolarimetry modes are in commissioning with observations including redundant half-wave plate pairs to be commissioned thereafter.¹⁰

⁹The PG0300 surface relief grating has been replaced with the PG0700 VPH grating as of November 2022 but has been included here as observations using the PG0300 are used in later sections.

¹⁰Commission status sighted from the latest ‘Polarimetry Observers Guide’ (2024).

Linear (°)		Linear-Hi (°)		Circular (°)		Circular-Hi (°)		All Stokes (°)	
$\frac{1}{2}$ wave	$\frac{1}{4}$ wave	$\frac{1}{2}$ wave	$\frac{1}{4}$ wave	$\frac{1}{2}$ wave	$\frac{1}{4}$ wave	$\frac{1}{2}$ wave	$\frac{1}{4}$ wave	$\frac{1}{2}$ wave	$\frac{1}{4}$ wave
0	-	0	-	0	45	0	45	0	0
45	-	45	-	0	-45	0	-45	45	0
22.5	-	22.5	-			22.5	-45	22.5	0
67.5	-	67.5	-			22.5	45	67.5	0
	-	11.25	-			45	45	0	45
	-	56.25	-			45	-45	0	-45
	-	33.75	-			67.5	-45		
		78.75	-			67.5	45		

Table 2.2: Spectropolarimetry waveplate patterns defined for the RSS. The stated angles refer to the angle of the waveplate’s optical axis from the perpendicular of the dispersion axis. Table adapted from the SALT call for proposals (2023).

2.5.1 POLSALT

POLSALT is the current reduction package being developed within SAAO/SALT as the official reduction pipeline for spectropolarimetric data taken using SALTs RSS.¹¹ Newer versions of the software include a Graphical User Interface (GUI) as well as limited interactivity during key steps in the reduction process. Below we summarize the reduction steps for the “beta version” [23 January 2020] which was adapted in this study.

The steps that make up the reduction pipeline include basic CCD reductions, wavelength calibrations, background subtraction and spectral extraction, raw stokes calculations, final stokes calculations, and visualization of the results. Each step is crucial for good results and thus briefly discussed (a detailed documentation for the reduction steps and purpose may be found at the POLSALT github wiki):

Basic CCD reductions: Basic CCD reductions are run via `imred.py` and apply basic reductions to the raw data necessary before any calibrations may be done. These corrections include overscan subtractions, gain corrections, crosstalk corrections, and mosaicking as well as attaching the bad pixel maps and pixel variance information. Files with basic reductions performed have “mxgbp” prepended to their names. As of February 2022, the reduction step is automatically run for all RSS spectropolarimetric observations as part of the default SALT basic reduction pipeline that is run each day.

Wavelength calibrations: Wavelength calibration and cosmic-ray rejection is performed via `specpolwavmap.py` and separately calibrates the *O*- and *E*-beams, based on the arc frames, and applies a simple cosmic-ray rejection for all science frames. This step is interactive and allows the user to individually fit wavelength calibration maps to each beam. The importance of good correlation between both beams has been touched on previously and will be further discussed in § 3.1. The wavelength calibrated results are saved as an additional extension to each science FITS file, which are prefixed with a “w”, and the *O*- and *E*-beams of the extensions are split into their own sub-extensions.

Spectral extraction: The background subtraction and spectral extraction are run via `specpolextract_dev.py` which corrects for the beam-splitter distortion and tilt, performs

¹¹POLSALT is made freely available via the POLSALT GitHub repository, available at <https://github.com/saltastro/polsalt>. It is strongly advised to follow the wiki for installation instructions.

sky subtraction, and extracts a one dimensional wavelength dependent spectrum for each beam extension. This step is interactive and, using the brightest trace in the images, allows the user to define regions which span the wavelength axis and which define the background and trace regions for the sky subtraction and spectral extraction. Files with corrections applied are saved with “c” prepended to their names and files which contain the extracted one dimensional spectrum have “e” further prepended to their names.

Raw stokes calculations: Raw stokes calculations are performed via **specpolraw-stokes_dev.py** and identify waveplate pairs for which the intensity, I , and a ‘raw stokes’ signal, S , are calculated as:

$$\begin{aligned} I &= \frac{1}{2}(O_1 + O_2 + E_1 + E_2) \\ S &= \frac{1}{2} \left[\left(\frac{O_1 - O_2}{O_1 + O_2} \right) - \left(\frac{E_1 - E_2}{E_1 + E_2} \right) \right]. \end{aligned} \quad (2.51)$$

The raw stokes signal is calculated as the normalized difference of the O - and E -beams, for a waveplate pair, taken perpendicular to one another. The files generated containing the raw stokes information have a very specific naming style, with most notably the pair of frames used being included.

Final stokes calculations: The Final stokes calculations are performed via **specpol-finalstokes.py** and, using the waveplate pattern along with the raw stokes signals, calibrates for polarimetric zero-point and waveplate efficiency calibrations and calculates the final stokes parameters. Before the final stokes calculations are performed, data culling is applied to the raw stokes to eliminate outlier results which may arise due to, for example, atmospheric conditions. Data culling compares observation cycles against one another, compares the deviation of the means which estimate the systematic polarization baseline fluctuations (due to imperfections in repeatability), and performs a chi-squared analysis to eliminate outliers.

Visualization: Plotting the results of the spectropolarimetric reduction process uses **specpolview.py** and generates a plot of the Intensity, Linear Polarization (%), and Equatorial Polarization Angle (°) against a shared wavelength axis, as seen in Figure 2.20. This step is interactive and various options, such as the wavelength range, binning, etc., are available.

Post-processing analysis: Generally, the plot of the spectropolarimetric results is the stopping point for most reduction procedures as it contains or creates the desired results. However, additional tools exist which may be used after the polarization reductions have been completed, and which are not represented in the GUI, namely, flux calibration and synthetic filtering.

Flux-calibrations are performed via **specpolflux.py** and are only intended for shape corrections of the spectrum. Additionally, the flux database file must exist for the standard observed and must be copied over to the working science directory.

Synthetic filtering is calculated via **specpolfilter.py** and computes the synthetically filtered polarization results. The filters which can be synthesized are the Johnson U , B , and V filter curves from the SALTICAM filters, as well as the Cousins R and I filter curves, along with any user defined wavelength dependent throughput.

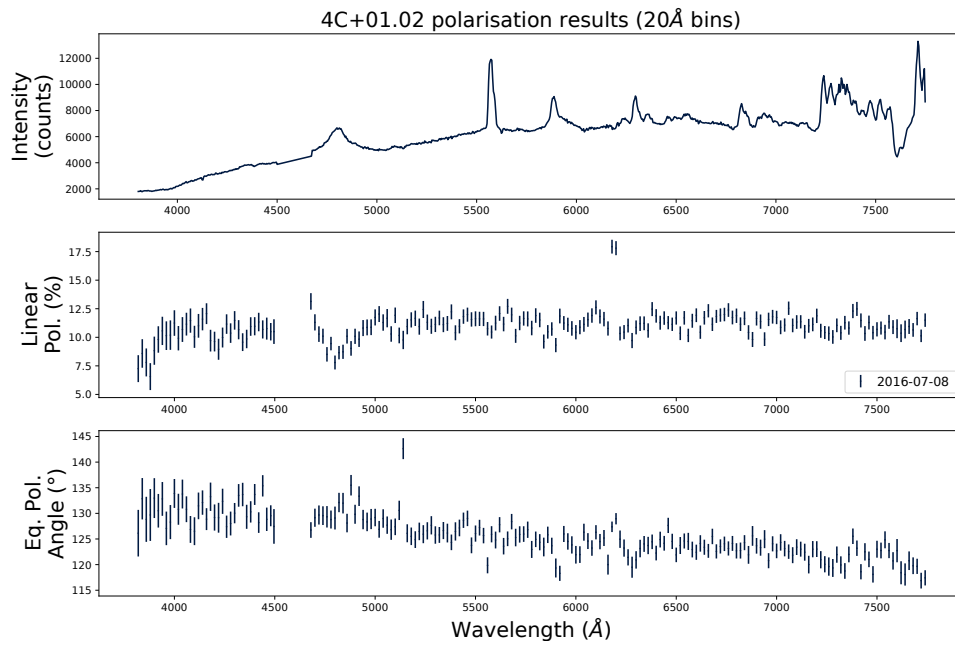


Figure 2.20: A typical plot resulting from the reduction process. Figure adapted from (Cooper et al., 2022)

Chapter 3

Developed Tools

This chapter contains an overview of why supplementary tools were deemed necessary for an already complete reduction process (§ 3.1), which aspects of the reduction process have been altered, replaced, or added (§ 3.2, 3.3), and finally what an updated reduction process consists of using a combination of all software.

3.1 Limitations of POLSALT and the Need for a Supplementary Tool

The creation of supplementary tools for POLSALT spectropolarimetric reductions stem from, primarily, the limitations of the wavelength calibration phase and a need for a way to compare wavelength solutions across matching *O* and *E* polarization beams. Due to the time-consuming process of recalibrating the wavelength solutions it is not feasible to perform the wavelength calibrations time and time again for any amount of reductions larger than a handful of observations.

One solution is to use a well established tool to perform the wavelength calibration, one which allows for rapid recalibrations as well as provides a familiar interface with which the user can analyze their wavelength solution. IRAF provides this familiar environment and reliability, even considering it's age and lack of further development. Unfortunately, IRAF is unable to parse the files as is and a need for formatting is necessary for integration purposes. This restructuring works both ways as once the IRAF reductions are complete the format must be reformatted to match that of the POLSALT output such that reductions can carry on in POLSALT.

TODO: Can mention other faults very briefly, but the main takeaway should be the need for a way to do the wavelength calibration with more control as well as the need to check the O/E beam wavelength calibrations against one another (since very accurate wavelength calibration necessary for stokes parameter calculations)

3.2 Wavelength calibrations using the Supplementary Pipeline and IRAF

3.2.1 Splitting the uncalibrated wavelength files

3.2.2 IRAF wavelength calibration

3.2.3 Joining the wavelength calibrated files

3.3 Additional Tools

3.3.1 Cross correlation

3.3.2 Skyline comparisons

3.4 General Reduction Procedure

Chapter 4

Testing

TODO: Add all tests done and comparisons.

- 3C 279
- 4C+01.02
- David data (not in next section publications because still during pipeline development. Reductions done through polysalt, but after publication used as preliminary testing data)

Chapter 5

Science Applications

TODO: short introduction to chapter contents

5.1 Application to Spectropolarimetric Standards

TODO: Spectropolarimetric standards (4 highly polarised, 2 non-polarised)

- Background on objects
- Reductions
- Actual results - comparison of polysalt results to supplementary pipeline results
- Science results, what the results can tell us and why it is useful, also comparison of results to FORS1/2 published data, focus on the polarisation results

5.2 Application in publications

TODO: Summary of results from papers in appendix.

- Hester paper(s)
- Joleen proceedings and work
- My proceedings

TODO: 3C 279 and 4C+01.02

- Give Background on objects, Reduction steps, and Science results (what the results can tell us and why it is useful)
- (comparison of polysalt results to supplementary pipeline results will be in testing)

Chapter 6

Conclusions

TODO: A summary of the dissertation, main focus on the results and that the supplementary pipeline is a success since it allows an alternate method using IRAF to wavelength calibrate the polysalt data.

Acknowledgements

I hereby acknowledge and express my sincere gratitude to the following parties for their valuable contributions:

- **TODO: Add acknowledgements!**

List of Acronyms

ADC	Analog-to-Digital Converter
CCD	Charged-Coupled Device
CMOS	Complementary Metal-Oxide-Semiconductor
GUI	Graphical User Interface
HET	Hobby-Eberly Telescope
HRS	High Resolution Spectrograph
NIR	Near Infra-Red
NIRWALS	Near Infra-Red WAsburn Labs Spectrograph
RSS	Robert Stobie Spectrograph
S/N	Signal-to-Noise Ratio
SAAO	South African Astronomical Observatory
SALT	Southern African Large Telescope
SALTICAM	SALT Imaging Camera
UV	Ultraviolet
VPH	Volume Phase Holographic

Bibliography

R. R. J. Antonucci and J. S. Miller. Spectropolarimetry and the nature of NGC 1068. ApJ, 297:621–632, October 1985. doi: 10.1086/163559.

George B. Arfken and Hans J. Weber. Mathematical methods for physicists, 1999.

S. Bagnulo, M. Landolfi, J. D. Landstreet, E. Landi Degl’Innocenti, L. Fossati, and M. Sterzik. Stellar spectropolarimetry with retarder waveplate and beam splitter devices. Publications of the Astronomical Society of the Pacific, 121(883):993, aug 2009. doi: 10.1086/605654. URL <https://dx.doi.org/10.1086/605654>.

Erasmus Bartholinus. Experimenta crystalli islandici dis-diaclastici, quibus mira et insolita refractio detegitur (copenhagen, 1670). Edinburgh Philosophical Journal, 1:271, 1670.

D. Scott Birney, Guillermo Gonzalez, and David Oesper. Observational Astronomy - 2nd Edition. Cambridge University Press, 2006. doi: 10.2277/0521853702.

Janus D. Brink, Moses K. Mogotsi, Melanie Saayman, Nicolaas M. Van der Merwe, Jonathan Love, and Alrin Christians. Preparing the SALT for near-infrared observations. In Heather K. Marshall, Jason Spyromilio, and Tomonori Usuda, editors, Ground-based and Airborne Telescopes IX, volume 12182 of Society of Photo-Optical Instrumentation Engineers (SPIE) Conference Series, page 121822E, August 2022. doi: 10.1117/12.2627328.

David A. H. Buckley, Gerhard P. Swart, and Jacobus G. Meiring. Completion and commissioning of the Southern African Large Telescope. In Larry M. Stepp, editor, Society of Photo-Optical Instrumentation Engineers (SPIE) Conference Series, volume 6267 of Society of Photo-Optical Instrumentation Engineers (SPIE) Conference Series, page 62670Z, June 2006. doi: 10.1117/12.673750.

Christian Buil. CCD astronomy : construction and use of an astronomical CCD camera / Christian Buil ; translated and adapted from the French by Emmanuel and Barbara Davoust. Willmann-Bell, Richmond, Va, 1st english ed. edition, 1991. ISBN 0943396298.

Eric B. Burgh, Kenneth H. Nordsieck, Henry A. Kobulnicky, Ted B. Williams, Daragh O’Donoghue, Michael P. Smith, and Jeffrey W. Percival. Prime Focus Imaging Spectrograph for the Southern African Large Telescope: optical design. In Masanori Iye and Alan F. M. Moorwood, editors, Instrument Design and Performance for Optical/Infrared Ground-based Telescopes, volume 4841 of Society of Photo-Optical

- Instrumentation Engineers (SPIE) Conference Series, pages 1463–1471, March 2003. doi: 10.1117/12.460312.
- Subrahmanyan Chandrasekhar. Radiative transfer, 1950.
- Marshall H. Cohen. Genesis of the 1000-foot Arecibo dish. Journal of Astronomical History and Heritage, 12(2):141–152, July 2009.
- J. Cooper, B. van Soelen, and R. Britto. Development of tools for SALT/RSS spectropolarimetry reductions: application to the blazar 3C279. In High Energy Astrophysics in Southern Africa 2021, page 56, May 2022. doi: 10.22323/1.401.0056.
- E. Landi Degl’Innocenti, S. Bagnulo, and L. Fossati. Polarimetric standardization, 2006.
- Egidio Landi Degl’Innocenti. The physics of polarization. Proceedings of the International Astronomical Union, 10(S305):1–1, 2014.
- Egidio Landi Degl’Innocenti and M. Landolfi. Polarization in Spectral Lines, volume 307. Springer Dordrecht, 2004. doi: 10.1007/978-1-4020-2415-3.
- Königlich Bayerische Akademie der Wissenschaften. Denkschriften der Königlichen Akademie der Wissenschaften zu München für das Jahre 1820 und 1821, volume 8. Die Akademie, 1824. URL <https://books.google.co.za/books?id=k-EAAAAAYAAJ>.
- J. F. Donati, M. Semel, B. D. Carter, D. E. Rees, and A. Collier Cameron. Spectropolarimetric observations of active stars. MNRAS, 291(4):658–682, November 1997. doi: 10.1093/mnras/291.4.658.
- I. V. Florinsky and A. N. Pankratov. Digital terrain modeling with the chebyshev polynomials. Machine Learning and Data Analysis, 1(12):1647 – 1659, 2015. doi: 10.48550/ARXIV.1507.03960. URL <https://arxiv.org/abs/1507.03960>.
- Augustin Fresnel. Oeuvres completes d’Augustin Fresnel: 3. Imprimerie impériale, 1870.
- L. M. Freyhammer, M. I. Andersen, T. Arentoft, C. Sterken, and P. Nørregaard. On Cross-talk Correction of Images from Multiple-port CCDs. Experimental Astronomy, 12(3):147–162, January 2001. doi: 10.1023/A:1021820418263.
- David J Griffiths. Introduction to electrodynamics, 2005.
- George E. Hale. The Zeeman Effect in the Sun. PASP, 20(123):287, December 1908. doi: 10.1086/121847.
- George E. Hale. 16. On the Probable Existence of a Magnetic Field in Sun-Spots, pages 96–105. Harvard University Press, Cambridge, MA and London, England, 1979. ISBN 9780674366688. doi: doi:10.4159/harvard.9780674366688.c19. URL <https://doi.org/10.4159/harvard.9780674366688.c19>.
- P. D. Hale and G. W. Day. Stability of birefringent linear retarders(waveplates). Appl. Opt., 27(24):5146–5153, Dec 1988. doi: 10.1364/AO.27.005146. URL <https://opg.optica.org/ao/abstract.cfm?URI=ao-27-24-5146>.
- E. Hecht. Optics. Pearson Education, Incorporated, 2017. ISBN 9780133977226. URL <https://books.google.co.za/books?id=ZarLoQEACAAJ>.

- Steve B. Howell. Handbook of CCD Astronomy, volume 5. Cambridge University Press, 2006.
- Christian Huygens. Treatise on light, 1690. translated by Thompson, s. p., 1690. URL <https://www.gutenberg.org/files/14725/14725-h/14725-h.htm>.
- Mourad E. H. Ismail. Classical and Quantum Orthogonal Polynomials in One Variable. Encyclopedia of Mathematics and its Applications. Cambridge University Press, 2005. doi: 10.1017/CBO9781107325982.
- James Janesick, James T. Andrews, and Tom Elliott. Fundamental performance differences between CMOS and CCD imagers: Part 1. In David A. Dorn and Andrew D. Holland, editors, Society of Photo-Optical Instrumentation Engineers (SPIE) Conference Series, volume 6276 of Society of Photo-Optical Instrumentation Engineers (SPIE) Conference Series, page 62760M, June 2006. doi: 10.1117/12.678867.
- Christoph U. Keller. Instrumentation for astrophysical spectropolarimetry. Astrophysical Spectropolarimetry, 1:303–354, 2002.
- G. Kirchhoff and R. Bunsen. Chemische Analyse durch Spectralbeobachtungen. Annalen der Physik, 189(7):337–381, January 1861. doi: 10.1002/andp.18611890702.
- Henry A. Kobulnicky, Kenneth H. Nordsieck, Eric B. Burgh, Michael P. Smith, Jeffrey W. Percival, Ted B. Williams, and Darragh O’Donoghue. Prime focus imaging spectrograph for the Southern African large telescope: operational modes. In Masanori Iye and Alan F. M. Moorwood, editors, Instrument Design and Performance for Optical/Infrared Ground-based Telescopes, volume 4841 of Society of Photo-Optical Instrumentation Engineers (SPIE) Conference Series, pages 1634–1644, March 2003. doi: 10.1117/12.460315.
- Gerard Leng. Compression of aircraft aerodynamic database using multivariable chebyshev polynomials. Advances in Engineering Software, 28(2):133–141, 1997. ISSN 0965-9978. doi: [https://doi.org/10.1016/S0965-9978\(96\)00043-9](https://doi.org/10.1016/S0965-9978(96)00043-9). URL <https://www.sciencedirect.com/science/article/pii/S0965997896000439>.
- Dave Litwiller. Ccd vs. cmos. Photonics spectra, 35(1):154–158, 2001.
- Dongyue Liu and Bryan M. Hennelly. Improved wavelength calibration by modeling the spectrometer. Applied Spectroscopy, 76(11):1283–1299, 2022. doi: 10.1177/00037028221111796. URL <https://doi.org/10.1177/00037028221111796>. PMID: 35726593.
- Etienne L. Malus. Sur une propriété de la lumière réfléchie. Mém. Phys. Chim. Soc. d’Arcueil, 2:143–158, 1809.
- I. Newton and W. Innys. Opticks:: Or, A Treatise of the Reflections, Refractions, Inflections and Colours of Light. Opticks:: Or, A Treatise of the Reflections, Refractions, Inflections and Colours of Light. William Innys at the West-End of St. Paul’s., 1730. URL <https://books.google.co.za/books?id=GnAFAAAAQAAJ>.
- Kenneth H. Nordsieck, Kurt P. Jaehnig, Eric B. Burgh, Henry A. Kobulnicky, Jeffrey W. Percival, and Michael P. Smith. Instrumentation for high-resolution spectropolarimetry

- in the visible and far-ultraviolet. In Silvano Fineschi, editor, Polarimetry in Astronomy, volume 4843 of Society of Photo-Optical Instrumentation Engineers (SPIE) Conference Series, pages 170–179, February 2003. doi: 10.1117/12.459288.
- D. O’Donoghue, D. A. H. Buckley, L. A. Balona, D. Bester, L. Botha, J. Brink, D. B. Carter, P. A. Charles, A. Christians, F. Ebrahim, R. Emmerich, W. Esterhuyse, G. P. Evans, C. Fourie, P. Fourie, H. Gajjar, M. Gordon, C. Gumede, M. de Kock, A. Koeslag, W. P. Koorts, H. Kriel, F. Marang, J. G. Meiring, J. W. Menzies, P. Menzies, D. Metcalfe, B. Meyer, L. Nel, J. O’Connor, F. Osman, C. Du Plessis, H. Rall, A. Riddick, E. Romero-Colmenero, S. B. Potter, C. Sass, H. Schalekamp, N. Sessions, S. Siyengo, V. Sopela, H. Steyn, J. Stoffels, J. Scholtz, G. Swart, A. Swat, J. Swiegers, T. Tiheli, P. Vaisanen, W. Whittaker, and F. van Wyk. First science with the Southern African Large Telescope: peering at the accreting polar caps of the eclipsing polar SDSS J015543.40+002807.2. MNRAS, 372(1):151–162, October 2006. doi: 10.1111/j.1365-2966.2006.10834.x.
- Darragh O’Donoghue. Correction of spherical aberration in the Southern African Large Telescope (SALT). In Philippe Dierickx, editor, Optical Design, Materials, Fabrication, and Maintenance, volume 4003 of Society of Photo-Optical Instrumentation Engineers (SPIE) Conference Series, pages 363–372, July 2000. doi: 10.1117/12.391526.
- Darragh O’Donoghue. Atmospheric dispersion corrector for the Southern African Large Telescope (SALT). In Richard G. Bingham and David D. Walker, editors, Large Lenses and Prisms, volume 4411 of Society of Photo-Optical Instrumentation Engineers (SPIE) Conference Series, pages 79–84, February 2002. doi: 10.1117/12.454874.
- Ferdinando Patat and Martino Romaniello. Error Analysis for Dual-Beam Optical Linear Polarimetry. PASP, 118(839):146–161, January 2006. doi: 10.1086/497581.
- Alba Peinado, Angel Lizana, Josep Vidal, Claudio Iemmi, and Juan Campos. Optimization and performance criteria of a stokes polarimeter based on two variable retarders. Opt. Express, 18(10):9815–9830, May 2010. doi: 10.1364/OE.18.009815. URL <https://opg.optica.org/oe/abstract.cfm?URI=oe-18-10-9815>.
- W. H. Press, S. A. Teukolsky, W. T. Vetterling, and B. P. Flannery. Numerical Recipes 3rd Edition: The Art of Scientific Computing. Cambridge University Press, 2007. ISBN 9780521880688. URL <https://books.google.co.za/books?id=1aA0dzK3FegC>.
- J. R. Priebe. Operational form of the mueller matrices. J. Opt. Soc. Am., 59(2):176–180, Feb 1969. doi: 10.1364/JOSA.59.000176. URL <https://opg.optica.org/abstract.cfm?URI=josa-59-2-176>.
- Lawrence W. Ramsey, M. T. Adams, Thomas G. Barnes, John A. Booth, Mark E. Cornell, James R. Fowler, Niall I. Gaffney, John W. Glaspey, John M. Good, Gary J. Hill, Philip W. Kelton, Victor L. Krabbendam, L. Long, Phillip J. MacQueen, Frank B. Ray, Randall L. Ricklefs, J. Sage, Thomas A. Sebring, W. J. Spiesman, and M. Steiner. Early performance and present status of the Hobby-Eberly Telescope. In Larry M. Stepp, editor, Advanced Technology Optical/IR Telescopes VI, volume 3352 of Society of Photo-Optical Instrumentation Engineers (SPIE) Conference Series, pages 34–42, August 1998. doi: 10.1117/12.319287.

- Maria C. Simon. Wollaston prism with large split angle. *Appl. Opt.*, 25(3):369–376, Feb 1986. doi: 10.1364/AO.25.000369. URL <https://opg.optica.org/ao/abstract.cfm?URI=ao-25-3-369>.
- G. G. Stokes. On the Composition and Resolution of Streams of Polarized Light from different Sources. *Transactions of the Cambridge Philosophical Society*, 9:399, January 1851.
- Stephen F. Tonkin. *Practical Amateur Spectroscopy*. The Patrick Moore Practical Astronomy Series. Springer London, 2013. ISBN 9781447101277. URL <https://books.google.fr/books?id=b2fgBwAAQBAJ>.
- L. Wang and J. C. Wheeler. Spectropolarimetry of supernovae. *ARA&A*, 46:433–474, September 2008. doi: 10.1146/annurev.astro.46.060407.145139.
- Marsha J. Wolf, Matthew A. Bershad, Michael P. Smith, Kurt P. Jaehnig, Jeffrey W. Percival, Joshua E. Oppor, Mark P. Mulligan, and Ron J. Koch. Laboratory performance and commissioning status of the SALT NIR integral field spectrograph. In Christopher J. Evans, Julia J. Bryant, and Kentaro Motohara, editors, *Ground-based and Airborne Instrumentation for Astronomy IX*, volume 12184 of *Society of Photo-Optical Instrumentation Engineers (SPIE) Conference Series*, page 1218407, August 2022. doi: 10.1117/12.2630242.
- William H. Wollaston. XII. A Method of Examining Refractive and Dispersive Powers, by Prismatic Reflection. *Philosophical Transactions of the Royal Society of London Series I*, 92:365–380, January 1802. doi: 10.1098/rstl.1802.0013.